




Impact of chlorite dehydration on intermediate-depth earthquakes in subducting slabs

Dohyun Kim ^{1,2}, Haemyeong Jung ¹✉ & Jungjin Lee ¹

Intermediate-depth earthquakes are common in the double seismic structures of many subduction zones under high pressures (~1–4 GPa). Serpentine dehydration exhibits well-established links with double seismic zone earthquakes. Additionally, dehydration of several hydrous minerals including lawsonite and chlorite underlying the upper and lower layers, respectively, may be responsible for intermediate-depth earthquakes. Here, we present experimental evidence suggesting that chlorite dehydration can trigger intermediate-depth earthquakes at the lower plane (~700 °C). We conducted deformation experiments on chlorite peridotite under high-pressure (0.5–2.5 GPa) and high-temperature (500–750 °C) using a modified Griggs apparatus. Experiments revealed the presence of faults in samples that had undergone partial chlorite dehydration with the presence of the dehydration product Ca-amphibole along these faults. Our findings confirm, together with correlation studies between seismicity and mineral stability, that a part of intermediate-depth seismicity in the lower plane of double seismic zones can be attributed to chlorite dehydration.

¹Tectonophysics Laboratory, School of Earth and Environmental Sciences, Seoul National University, Seoul 08826, Republic of Korea. ²Present address: Division of Earth Sciences, Korea Polar Research Institute, Incheon 21990, Republic of Korea. ✉email: hjung@snu.ac.kr

Intermediate-depth earthquakes at depths of 50–300 km have been documented in double seismic zones of many subduction zones^{1–7}. However, brittle deformation is rare in high-pressure, high-temperature (P - T) conditions^{8–10}. Several triggering and rupture mechanisms have been proposed to explain intermediate-depth earthquakes. Dehydration embrittlement^{11–14}, reaction-induced grain size reduction^{15,16}, and stress transfer models (dehydration-driven stress transfer: DDST, transformation-driven stress transfer: TDST)^{17–19} are representative triggering mechanisms. Rupture mechanisms include self-localising thermal runaway^{16,20–22}, melt-assisted lubrication^{23,24}, thermal pressurisation^{25,26}, and transformational faulting^{27,28}. The triggering mechanism involving dehydration of hydrous minerals such as serpentine in the upper mantle^{12,19} and lawsonite in the subducting oceanic crust¹³ has been considered as a plausible explanation for intermediate-depth earthquakes in subducting slabs of double seismic zones^{4,8,9,11,12,14,17–19,29–32}. Although intermediate-depth earthquakes in the lower plane of the double seismic zone (Fig. 1) can be attributed to serpentine dehydration mechanisms (including DDST^{19,33}) at low temperature^{17–19,34}, the seismicity in this region, particularly at high temperature (~ 700 °C), may be attributed to the dehydration of other hydrous minerals^{10,34–36}.

Chlorite exhibits a wide stability range in subduction zones under high P - T conditions^{11,37} (Fig. 1). Chlorite peridotite is stable in the lower layer of double seismic zones. Chlorite has also

been identified as a key mineral for water transport to the mantle and fluid transfer reactions in subduction zones^{38–42}. Based on laboratory experiments and seismicity correlation studies, researchers have inferred that seismicity in the lower plane of double seismic zones could be linked to the dehydration of hydrous minerals, including serpentine and chlorite^{11,17,37,39}. In this study, we aimed to understand the mechanism of intermediate-depth earthquakes under high-temperature conditions in subduction zones by conducting deformation experiments on chlorite peridotite under the high P - T conditions of subducting slabs. Previous studies have predominantly concentrated on serpentine dehydration to understand the intermediate-depth seismicity of subducting slabs^{4,12,19,32}, with some also highlighting the role of chlorite in triggering such seismicity^{1,17}. Our experimental findings indicate that chlorite peridotite dehydration causes intermediate-depth earthquakes in the upper and lower plane of double seismic zones at high temperatures.

Results

Table 1 presents the results of deformation experiments on chlorite peridotite (as described in the Methods). Fourteen simple-shear experiments were conducted (Supplementary Fig. 1) in a modified Griggs apparatus under a high confining pressure of approximately 2 GPa (pressure at a depth of ~ 60 km) and high-temperature conditions (500–750 °C) at a constant longitudinal strain rate of 2.7 – $6.9 \times 10^{-6} \text{ s}^{-1}$. The previously known reactions of chlorite (e.g., chlorite = forsterite + pyrope + spinel + H_2O) occurred with synthetic starting material^{43,44}. In this study, the theoretical stability fields and reaction formula of chlorite and amphibole were calculated based on pseudosections using Theriak-Domino software (Fig. 2a, b), considering the modal composition of the natural starting material (chlorite peridotite). The expected product of the dehydration reaction under these conditions is amphibole: chlorite + pyroxene + Na-phlogopite + vesuvianite = olivine + amphibole + H_2O . Minor minerals such as vesuvianite and phlogopite were difficult to observe in the starting material because of their extremely low volume percentage ($\sim 0.5\%$). The fluid-dependent stability field change under the temperature conditions of this study⁴⁵ may explain why vesuvianite was not detected. In the five samples represented by red stars in Fig. 2a, b, faults were observed within the coexistence zone of chlorite and amphibole under high pressures (1.5–2.5 GPa).

Fluid inclusion trails were observed in the faulted samples (Fig. 2c) for both positive and negative volume changes (Table 1). Fluid inclusions, which were not observed in the starting material, are interpreted as evidence of chlorite dehydration in the experimentally deformed samples. Fluids from the dehydration of chlorite left fluid inclusion trails inside olivine grains, and the trails were aligned subparallel ($\leq 30^\circ$) to σ_1 —the maximum principal stress orientation of the deformation experiment (Fig. 2c and Supplementary Fig. 1). The aligned fluid inclusions were formed after Mode-I cracks that were subparallel ($\leq 30^\circ$) to maximum principal stress orientation σ_1 (Fig. 2d).

In samples in which no fault could be observed, strain localisation resulted in the layering of the chlorite grains. The deformation can be accommodated by shearing along the basal plane of well-oriented chlorite crystals (Fig. 3a). However, for samples with faults, chlorite sheets and olivine grains at three high-temperature conditions were cut by a fault under high pressures (1.5–2.5 GPa; Fig. 4a, b, and d; Table 1). A macroscopic fault is shown in Fig. 4a; a fault gouge that developed at 2.5 GPa and 750 °C is shown in Fig. 4b. A fine-grained dehydration product of chlorite was found along the fault gouge (Fig. 4c), as revealed by

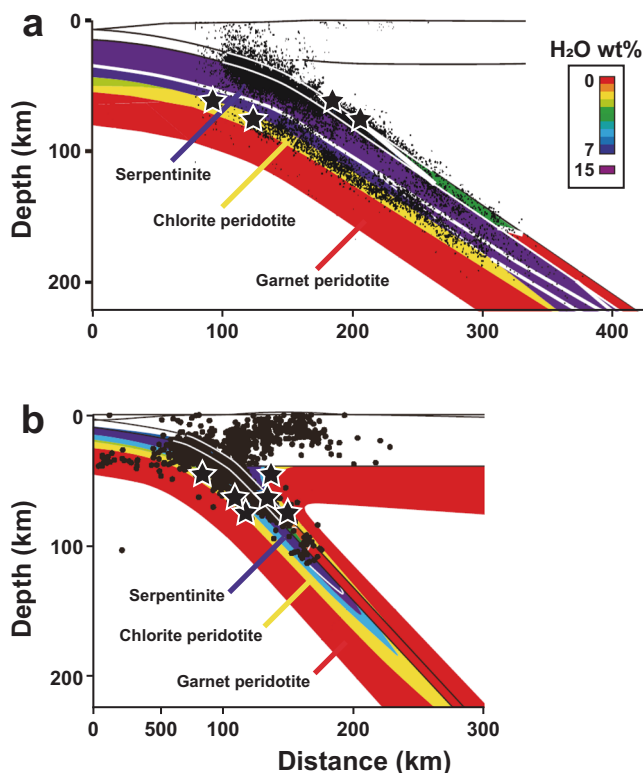


Fig. 1 Seismicity, stability fields of peridotite and serpentine, and experimental conditions in subduction zones. Two types of subduction zones (modified after Hacker, et al.¹¹), and experimental conditions of this study. **a** Cold (type I) subduction zone of northern Honshu, Japan. Seismicity is represented by black dots. The instability of chlorite would explain a fraction of the seismicity (around the transition between the yellow and red area zones). **b** Warm (type II) subduction zone of Costa Rica. Black stars indicate where samples were faulted and partial dehydration of chlorite was observed. Black stars for the condition of $P = 1.5$ GPa and $T = 650$ °C (samples JH138 and JH218) only match the geotherm of warm (type II) subduction zone (b)³⁹.

Table 1 Experimental conditions and results for deformation experiments on chlorite peridotite.

Sample	Pressure (GPa)	Temperature (°C)	Shear strain (γ)	Strain rate (s^{-1})	Maximum differential stress (MPa)	Fault development*	Inverse Clapeyron slope & volume change
JH101	0.5	650 ± 15	2.1 ± 0.5	2.65×10^{-6}	254 ± 15	X	>0
JH127	1.0	650 ± 15	3.5 ± 0.8	6.30×10^{-6}	120 ± 20	X	>0
JH100	1.0	720 ± 20	2.1 ± 0.5	5.48×10^{-6}	131 ± 20	X	>0
JH138	1.5	650 ± 15	3.3 ± 0.8	6.26×10^{-6}	352 ± 35	O	>0
JH218	1.5	650 ± 15	3.1 ± 0.8	6.03×10^{-6}	415 ± 35	O	>0
JH146	2.0	500 ± 10	3.3 ± 0.8	6.90×10^{-6}	354 ± 20	X	0
JH154	2.0	570 ± 10	2.8 ± 0.6	6.41×10^{-6}	259 ± 15	X	0
JH139	2.0	600 ± 10	3.8 ± 0.9	6.19×10^{-6}	346 ± 15	X	0
JH140	2.0	650 ± 15	3.8 ± 0.9	6.36×10^{-6}	173 ± 20	O	0
JH228	2.0	730 ± 20	3.5 ± 0.8	7.33×10^{-6}	489 ± 35	O	0
JH156	2.5	540 ± 10	1.6 ± 0.3	6.53×10^{-6}	238 ± 20	X	<0
JH152	2.5	630 ± 10	4.0 ± 1.0	6.51×10^{-6}	171 ± 20	X	<0
JH221	2.5	690 ± 15	2.1 ± 0.5	6.81×10^{-6}	130 ± 20	X	<0
JH225	2.5	750 ± 20	4.9 ± 1.5	7.12×10^{-6}	169 ± 20	O	<0

*Faulted (O) or unfaulted (X) samples were determined by measurable displacements observed by optical and electron microscope.

energy dispersive spectrometer (EDS) mapping of the deformed sample. Ca was distributed along the fault. Figure 4d shows the optical microscope image of the fault developed at 1.5 GPa and 650 °C. The EDS mapping images of the area (Fig. 4d) are shown in Fig. 4e and f; chlorite was Al-rich (Fig. 4e). We found a thin Ca-rich zone along the fault (Fig. 4f). The only mineral containing Ca in the starting material was clinopyroxene, with a bulk composition of 3%. Data from a field-emission electron probe microanalyser (FE-EPMA) revealed that the dehydration product containing Ca was amphibole (Supplementary Table 1), which was classified as tremolite: $Ca_{2.1}(Mg_{4.9}Fe_{0.2})Si_{8.1}O_{22}(OH)_2$ (Supplementary Table 1).

Herein, the stress–strain curves for experimental samples are shown in Supplementary Fig. 2. The stress–strain curves for the unfaulted samples showed a regular plastic deformation (e.g., samples JH146 and JH139). However, faulted samples showed marked stress drop after peak stress at high temperatures of 650–750 °C (e.g., samples JH140, JH218, and JH225) (Supplementary Fig. 2).

In summary, shear deformation experiments on chlorite peridotite were performed under high P - T conditions in this study, and faults were found (Fig. 4). At high pressures (1.5, 2.0, and 2.5 GPa) and temperatures (≥ 650 °C), Ca-amphibole was found along the faults, which is one of the dehydration products of chlorite (Fig. 4c, f). The microstructures of the faults exhibited slight differences in response to volume changes. Thin and sharp faults were observed under positive Clapeyron slope ($\Delta V > 0$) (Figs. 2a and 4f), while thick fault gouges developed under negative Clapeyron slope ($\Delta V < 0$) (Figs. 2a and 4c).

Discussion

Despite the risk of two-dimensional observations of three-dimensional structures and the inconsistency between theoretical pseudosections and experimental results^{17,34,37,46} (Supplementary Fig. 3), faulted samples showed fluid inclusions, partial chlorite dehydration, and a well identifiable dehydration product (Ca-amphibole). Our results indicate that chlorite dehydration likely contributes to seismicity under double seismic zone conditions. Partial chlorite dehydration, resulting in stable chlorite, could be explained by the other reactive phases in low fractions before actual instability ($T > 850$ °C under $P = 1.5$ – 2.5 GPa)¹⁷. Notably, no serpentine (antigorite) was detected in the starting material or faults of the experimental samples. It might be present as a minor mineral, akin to vesuvianite and phlogopite in the

starting material. Consequently, the influence of serpentine dehydration was not a factor under consideration in this study, given its absence in faults. However, considering the relatively low temperatures in the vicinity of ~ 500 °C (Supplementary Fig. 4), it is imperative to account for local equilibria within serpentinised faults.

Dehydration embrittlement was linked to positive volume change ($\Delta V > 0$) in dehydration reactions^{47,48}. Jung, et al.¹² demonstrated experimentally, at high pressures up to 6 GPa, that dehydration of serpentine can make a fault under the negative volume change ($\Delta V < 0$), which could be applied under the depth great enough for intermediate-depth earthquakes. DDST/TDST could be a possible dehydration-induced mechanism under the conditions in which dehydration embrittlement is not plausible^{17–19,34}. Notably, pseudosections of our starting material revealed a transition from a positive to negative volume change in the chlorite dehydration reaction at approximately 2 GPa (~ 60 km depth) with increasing pressure (Fig. 2a). Our experimental results validate that chlorite dehydration and fault formation occur both under positive ($P < 2$ GPa) and negative ($P > 2$ GPa) volume change (Table 1). The occurrence of negative volume change can facilitate the creation of fluid pathways, further promoting dehydration⁴⁹.

Extreme deformation localisation involves both seismic and aseismic faulting events, including earthquakes, tremors, and slow-slips. The observed mobility of Ca ions and the formation of Ca-amphibole within faults, as a product of metamorphic transformation, can be attributed to increased diffusivity within transforming aggregates. Alternatively, transient melting and rapid crystallisation, phenomena expected during dynamic ruptures under pressure^{15,19,23,50–54} could be other possibilities. In both natural and experimental analogues, seismic ruptures under high pressures consistently exhibit transient lubrication, often manifested as dynamic melting and preserved as pseudotachylytes, along with the emission of elastic waves. Although there was no acoustic recording in this study, some melts may have solidified into glassy materials near faults. Notably, we identified such glassy materials (Supplementary Fig. 5a) adjacent to faults that exhibited no Kikuchi bands in the electron backscattered diffraction pattern (EBSP) (Supplementary Fig. 5b). This observation would be consistent with the rapid diffusion of large cations such as Ca.

Our observations revealed the presence of fine-grained dehydration products, specifically Ca-amphibole (Fig. 4). The presence of Ca-amphibole in faults documents coeval fluid percolation and faulting. Consequently, it becomes evident that intermediate-

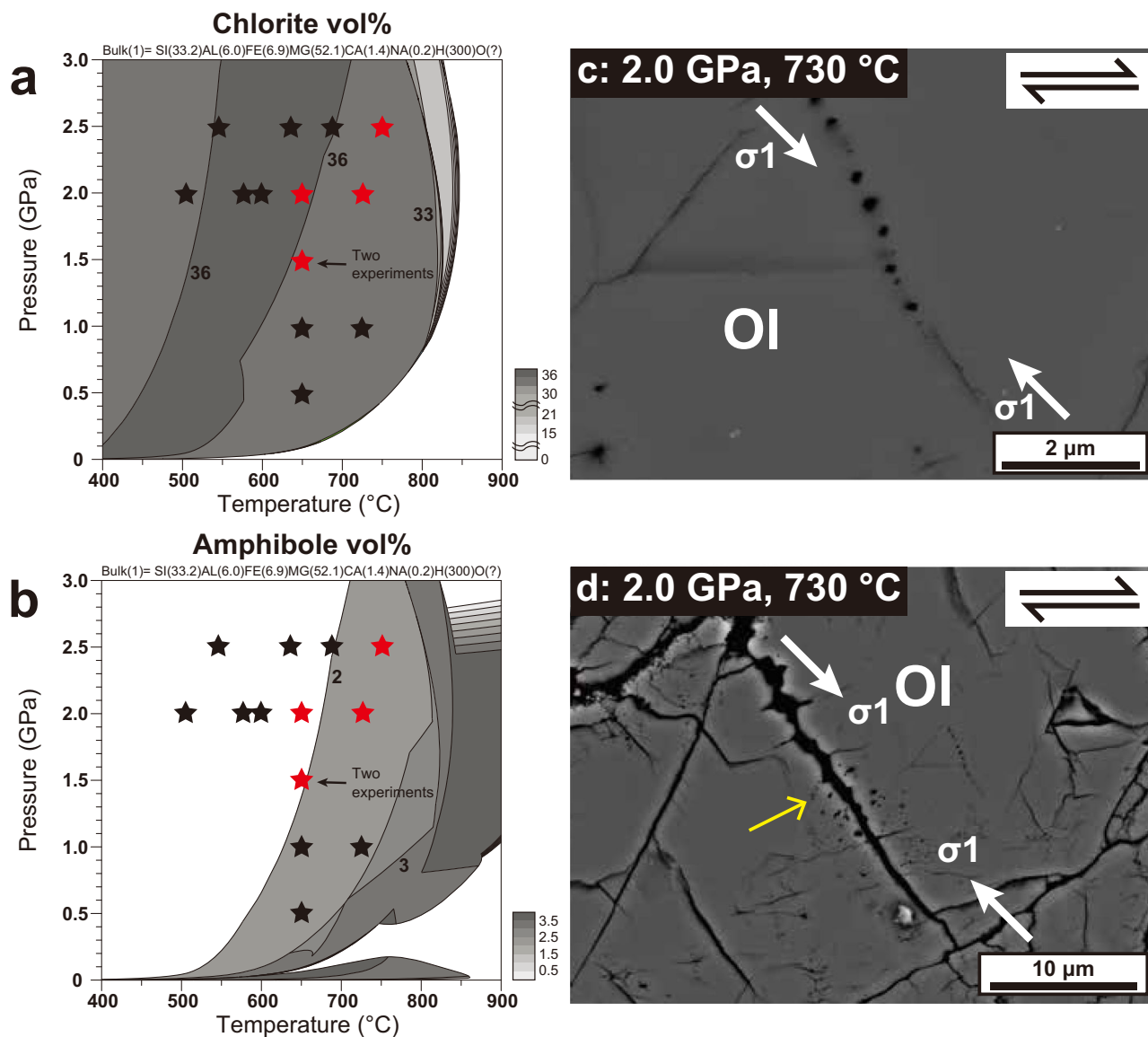


Fig. 2 Stability fields of minerals and fluid inclusion trail in olivine. **a, b** Stability fields and volume percentages of chlorite and amphibole using Theriak-Domino software⁶⁸, based on the starting material (chlorite peridotite⁶¹). O(?) in bulk represents auto calculation of oxygen content in Theriak-Domino software. The contour numbers on the figure represent the volume percentages of minerals. Stars represent experimental conditions of this study, and a fault and dehydration product of Ca-amphibole were observed on red stars. Fourteen experiments are represented by thirteen stars because samples JH138 and JH218 share the same *P-T* condition (1.5 GPa and 650 °C). Backscattered electron images (BEIs) show **c** a fluid inclusion trail and **d** Mode-I crack in olivine in a faulted sample deformed at 2.0 GPa and 730 °C (sample JH228). White arrows indicate orientation of maximum principal stress (σ_1), and the yellow arrow indicates a Mode-I crack that left a fluid inclusion trail. Ol: olivine.

depth earthquakes may be triggered not only by conventional dehydration embrittlement but also by stress transfer mechanisms such as DDST/TDST via chlorite dehydration. Additionally, the phenomenon of thermal runaway instability^{16,20–22,55} with its potential to induce local dehydration, emerges as a plausible rupture mechanism. This inference aligns with our observations of fine-grained Ca-amphiboles following the dehydration of chlorite.

Intermediate-depth seismicity in subducting slabs has been observed in the double seismic zones of many subduction zones, including north-eastern Japan, Tonga, northern Chile, Alaska, Kamchatka, the Marianas, New Britain, Costa Rica, and the Kuriles, as well as within the remnants of subducted slabs^{7,11,31,34,49,56–58}. Type I double seismic zones are defined by a layer separation of ~20–40 km, which converges at a depth of ~200 km^{57,59}. This type of double seismic zone can be found in

regions such as north-eastern Japan, Kamchatka, the Kuriles, the Marianas, and Tonga^{57,59}. In contrast, type II double seismic zones are characterised by a layer separation of less than 15 km, which converges at a depth of ~150 km^{57,59}. Examples of type II double seismic zones include northern Chile, Alaska, New Britain, and Costa Rica^{57,59}. The upper-plane seismicity of double seismic zones has been attributed to the dehydration of hydrous minerals such as serpentine of the upper mantle^{12,29–31,34} and lawsonite of the subducting oceanic crust¹³. Similarly, the lower-plane seismicity within the double seismic zone has also been linked to dehydration mechanisms involving serpentine^{18,19,34}. However, the potential for dehydration of other hydrous minerals has been proposed in the context of the lower-plane seismicity of the double seismic zone^{4,9,11,13,31,57–59}.

Subduction zones that are categorised as “warm” or type II double seismic zones are known to release fluids at great

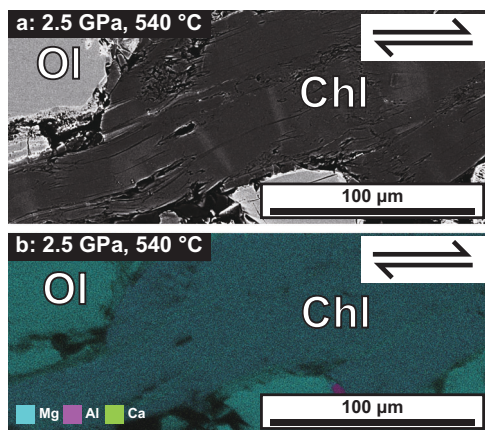


Fig. 3 BEI and energy dispersive spectrometer (EDS) mapping of an unfaulted sample. **a** Representative BEI of the sample without a fault deformed at 2.5 GPa and 540 °C (sample JH156). **b** Energy dispersive spectrometer (EDS) mapping image of the same area in **a** showing Mg and Al distribution, but no Ca distribution in the sample. Chl: chlorite; Ol: olivine.

depths^{39,41,59}. This characteristic makes it more likely for these zones to experience dehydration of hydrous minerals at larger depths. In addition, subduction zones that are considered “cold” or type I double seismic zones may still be able to deliver fluids to the deep mantle³⁸. There have been suggestions that this could occur in rock compositions that are rich in chlorite³⁸. Studies have proposed that the dehydration of chlorite can be a source of seismicity in cold (type I) subduction zones^{4,30,31,58}. Mineral dehydration has been suggested for both types of subduction zones^{1,17}.

The stability field of chlorite peridotite corresponds to the area of the lower plane of the double seismic zone (Fig. 1)^{4,7,11}. The *P-T* conditions of faulted chlorite peridotite samples in this study (1.5–2.5 GPa and 650–750 °C) correspond to both cold (type I) and warm (type II) double seismic zones, similar to the behavior of serpentine^{4,7,11,17,18,34} (Fig. 1). North-eastern Japan is the representative cold (type I) subduction zone^{4,11,56–58,60}, and Costa Rica is the representative warm (type II) subduction zone^{4,11,57}. Thus, most intermediate-depth earthquakes in double seismic zones can be explained by the dehydration of chlorite, serpentine, and other hydrous minerals^{10,17,34–36} in both the north-eastern Japan and Costa Rican subduction zones.

The samples that underwent deformation had ~31 vol.% of chlorite before deformation. After deformation, the samples had ~30 vol.% of chlorite and ~1 vol.% of dehydration product. Hacker, et al.⁴⁶ theoretically estimated a fraction of 10–35 vol.% of chlorite in peridotites of subducting slabs. Kim and Jung⁶¹ reported the presence of natural chlorite peridotites from Norway originating in the subduction zone, containing approximately 35 vol.% of chlorite. Similarly, Morales, et al.⁶² reported ~22 vol.% of chlorite in erupted mantle fragments, and Alt, et al.⁶³ also reported ~20 vol.% of chlorite in chlorite harzburgite that was exhumed from the subduction zone. Furthermore, Lee, et al.⁶⁴ reported an ultrahigh-pressure tectonic mélange from central Asia, which contained ~30 vol.% of chlorite. Therefore, in addition to serpentine dehydration, some subducting slabs with a chlorite volume percentage of approximately 30% may also undergo chlorite dehydration, potentially contributing to seismicity via mechanisms such as dehydration embrittlement and DDST/TDST.

Figure 1 shows representative examples of double seismic zones: north-eastern Japan for type I and Costa Rica for type II. The different depth limits of the two types can be attributed to the

subduction angle, oceanic plate age, slab temperature, plate thickness, convergence velocity, back-arc deformation patterns, and other factors^{7,17,57,59}. The *P-T* conditions, which exhibited partial dehydration of chlorite and faulting (1.5–2.5 GPa and 650–750 °C), agreed with the conditions observed in areas of seismicity in both the upper and lower planes of double seismic zones in cold (type I) north-eastern Japan and warm (type II) Costa Rica (Fig. 1) and are also applicable to other subduction zones^{11,37,58}. In contrast, dehydration of chlorite under low-pressure condition (1.5 GPa and 650 °C) was applicable to the high-temperature geotherm³⁹ of the warm (type II) double seismic zones (Fig. 1b).

Conclusions

In this study, deformation experiments of chlorite peridotite were conducted under high *P-T* conditions (0.5–2.5 GPa and 500–750 °C), representative of subduction zones. Faults developed and are filled with a dehydration product (Ca-amphibole) and an amorphous material suggesting dynamic melting of the chlorite peridotite. The results support that dehydration-induced faulting mechanisms (e.g., dehydration embrittlement or DDST/TDST) are applicable to not only well-known serpentine minerals, but also to chlorite to explain intermediate-depth earthquakes within subducting slabs.

Methods

Starting material. Chlorite peridotite⁶¹ from Almklovdaalen, Western Gneiss Region, southwest Norway, was used as the starting material. The modal composition of the starting material was olivine (60%), chlorite (31%), orthopyroxene (5%), clinopyroxene (3%), and garnet (1%). The chemical composition of chlorite was clinocllore ($\text{Mg}_{4.6}\text{Fe}^{2+}_{0.3}\text{Cr}_{0.1}\text{Al}(\text{Si}_3\text{Al})\text{O}_{10}(\text{OH})_8$), analysed using a JEOL JXA-8900R electron probe microanalyser (EPMA) at the National Center for Inter-university Research Facilities (NCIRF) at Seoul National University (SNU). For the EPMA setup, the acceleration voltage, working distance, current probe, and beam diameter were 15 kV, 10 mm, 20 nA, and 3 µm, respectively. The peak time was 10 s for Na and K and 20 s for the other elements. The background time was 5 s for Na and K and 10 s for the other elements.

Deformation experiment at high-pressure. Deformation experiments of chlorite peridotite were conducted under simple shear at high pressure (0.5–2.5 GPa) and temperature (500–750 °C) using a modified Griggs apparatus at the Tectonophysics Laboratory, School of Earth and Environmental Sciences (SEES) in SNU. Supplementary Fig. 1 shows the sample assembly used for shear deformation. The samples were core-drilled with a diameter of 3.1 mm and cut at 45°. They were placed between Al_2O_3 pistons inside the nickel capsule. A nickel foil was inserted in the middle of the sample—perpendicular to the shear plane—to measure the shear strain. An extremely weak solid (CsCl and NaCl) was used as a pressure medium to minimise the friction of the apparatus. The temperature was measured using two thermocouples (Pt-30%, Rh-70% and Pt-6%, Rh-94%) close to the top and bottom of the sample. The temperature differences recorded by the two thermocouples imply uncertainties of 10–20 °C. We used the temperature reading close to the bottom of the sample as an estimated sample temperature. Temperature was reported without correction for the pressure effect on the thermocouple electromotive force (emf). The pressure effect on thermocouple emf is less than ~10 °C at 2 GPa⁶⁵. Pressure was raised first to a desired value in ~12 h and kept constant. The uncertainty in pressure estimation is caused by the friction⁶⁶ and the application of a deviatoric stress and is less than ~10%. Confining pressure during experiments was constantly

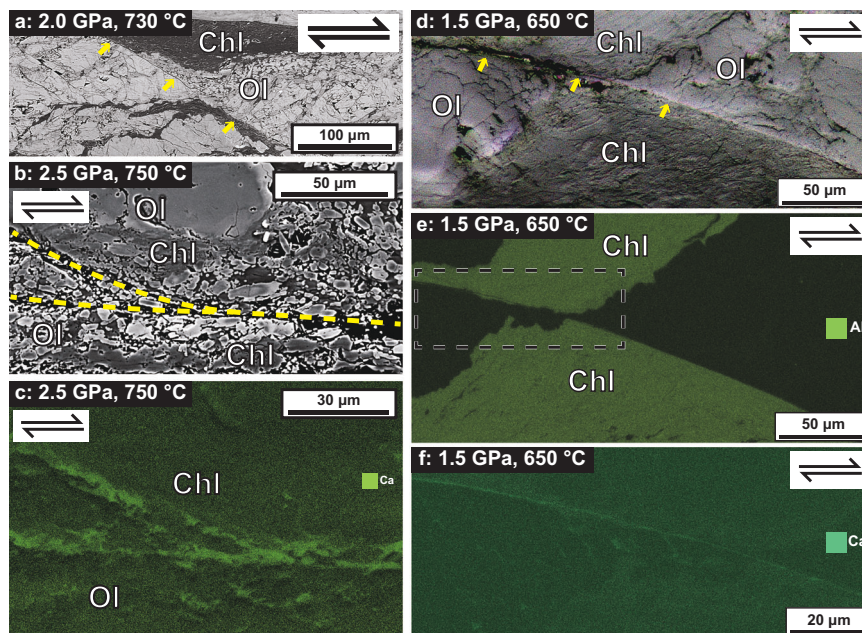


Fig. 4 BEI, EDS mapping, and optical photomicrograph of faulted samples. **a** BEI of deformed sample JH228 (2.0 GPa and 730 °C) showing a fault in chlorite peridotite (yellow arrows). **b** BEI and **c** EDS mapping image of deformed chlorite peridotite JH225 (2.5 GPa and 750 °C). Fault gouge (yellow dashed lines) and Ca distribution in Ca-amphiboles are shown in the same area. **d** Optical photomicrograph of deformed chlorite peridotite JH138 (1.5 GPa and 650 °C) with fault (yellow arrows) and **e** EDS mapping showing Al concentration-chlorite. **f** Magnified view of black dashed box in **e** showing Ca distribution in Ca-amphibole along the fault. Chl: chlorite; Ol: olivine.

controlled using a computer program installed at the Tectonophysics Laboratory, SEES, SNU. The uncertainty was less than ~ 50 MPa. The temperature was raised over ~ 1 h. After temperature stabilisation, a piston was advanced at constant rates of $2.7\text{--}6.9 \times 10^{-6} \text{ s}^{-1}$ using a stepping motor for a constant strain-rate deformation. Stress was measured with a load cell external to the apparatus; total friction in the system was measured by the force level on the moving (deformation) piston before it encountered the specimen. As a consequence, the reported strengths are upper bounds. Stress accuracy is estimated to be ± 35 MPa. After each deformation experiment, the sample was quenched to 27 °C by shutting off the power and the pressure was decreased for 12 h. Detailed procedures of the deformation experiments using this apparatus are presented in Ko and Jung⁶⁷.

Stability field and modal abundance. The stability field and volume percentage of chlorite and amphibole were calculated using an internally consistent dataset built from our up-to-date knowledge on mineral phases. We used Theriak-Domino software⁶⁸, which can manage thermodynamic data of mineral phases and can estimate their stable modal proportions and/or solid solutions in a given P-T range and a given bulk chemical composition, for the composition of the starting material (chlorite peridotite). In this study, for $P = 0\text{--}3$ GPa and $T = 400\text{--}900$ °C, the bulk composition of $\text{Na}_2\text{O} = 0.1$, $\text{CaO} = 1.5$, $\text{FeO} = 9.4$, $\text{MgO} = 39.6$, $\text{Al}_2\text{O}_3 = 5.8$, $\text{SiO}_2 = 37.6$ (wt. %) was used for the calculation assuming water saturation. The calculation was based on the modal composition of the starting material and the $\text{Na}_2\text{O}\text{--}\text{CaO}\text{--}\text{FeO}\text{--}\text{MgO}\text{--}\text{Al}_2\text{O}_3\text{--}\text{SiO}_2\text{--}\text{H}_2\text{O}$ (NCFMASH) model system, using the thermodynamic database of Holland and Powell⁶⁹ (tc55MnNCKFMASH file). The mineral phases considered in the model were chlorite⁷⁰, olivine⁷¹, antigorite⁷¹, diopside⁷², garnet⁷³, amphibole⁷⁴, orthopyroxene⁷⁵, phlogopite⁷¹, pargasite⁷¹, brucite⁷¹, hercynite⁷¹, clinohumite⁷¹, monticellite⁷¹, vesuvianite⁷¹, and phase A⁷¹.

Analytical methods. After the experiments, the samples were cut along the $x\text{--}z$ plane (x : shear direction, z : normal to the shear plane). The samples were polished with Syton 0.06 μm colloidal silica and observed using both an optical microscope and a field-emission scanning electron microscope (FE-SEM; JEOL JSM-7100F) housed at the SEES in SNU. EDS mapping attached to the FE-SEM equipment was used to visualise the element differences of the minerals. The acceleration voltage was 15 kV, and the working distance was 10 mm for FE-SEM. The step size of the EDS mapping was approximately 45–200 nm. AZtec software (Oxford Instruments) was used for the EDS analysis. A JEOL JXA-8530F FE-EPMA at the NCIRF at SNU was used to analyse the chemical composition of the minerals produced by the deformation experiments in the samples. For the FE-EPMA setup, the acceleration voltage, working distance, probe current, and beam diameter were 15 kV, 10 mm, 20 nA, and 3 μm , respectively. The peak time was 10 s for Na and K and 20 s for the other elements. The background time was set to 5 s for Na and K and 10 s for the remaining elements. Amphibole, the dehydration product of chlorite, was classified using an Excel spreadsheet of Locock⁷⁶, based on the chemical composition analysis of FE-EPMA.

Data availability

Data presented in the paper can be accessed via figshare at <https://doi.org/10.6084/m9.figshare.24495166>.

Received: 25 April 2023; Accepted: 20 November 2023;
Published online: 26 December 2023

References

1. Abers, G. A., Nakajima, J., van Keken, P. E., Kita, S. & Hacker, B. R. Thermal-petrological controls on the location of earthquakes within subducting plates. *Earth Planet. Sci. Lett.* **369**, 178–187 (2013).

2. Kita, S., Okada, T., Hasegawa, A., Nakajima, J. & Matsuzawa, T. Existence of interplane earthquakes and neutral stress boundary between the upper and lower planes of the double seismic zone beneath Tohoku and Hokkaido, northeastern Japan. *Tectonophysics* **496**, 68–82 (2010).
3. Kita, S., Okada, T., Nakajima, J., Matsuzawa, T. & Hasegawa, A. Existence of a seismic belt in the upper plane of the double seismic zone extending in the along-arc direction at depths of 70–100 km beneath NE Japan. *Geophys. Res. Lett.* **33**, L24310 (2006).
4. Hasegawa, A. & Nakajima, J. Seismic imaging of slab metamorphism and genesis of intermediate-depth intraslab earthquakes. *Prog. Earth Planet. Sci.* **4**, 1–31 (2017).
5. Hasegawa, A., Umino, N. & Takagi, A. Double-planed deep seismic zone and upper-mantle structure in the northeastern Japan arc. *Geophys. J. Int.* **54**, 281–296 (1978).
6. McGuire, J. J. & Wiens, D. A. A double seismic zone in New Britain and the morphology of the Solomon Plate at intermediate depths. *Geophys. Res. Lett.* **22**, 1965–1968 (1995).
7. Brudzinski, M. R., Thurber, C. H., Hacker, B. R. & Engdahl, E. R. Global prevalence of double Benioff zones. *Science* **316**, 1472–1474 (2007).
8. Green, H. W. & Houston, H. The mechanics of deep earthquakes. *Ann. Rev. Earth Planet. Sci.* **23**, 169–213 (1995).
9. Kirby, S. H. Interslab earthquakes and phase changes in subducting lithosphere. *Rev. Geophys.* **33**, 287–297 (1995).
10. Frohlich, C. *Deep earthquakes*. (Cambridge University Press, 2006).
11. Hacker, B. R., Peacock, S. M., Abers, G. A. & Holloway, S. D. Subduction factory 2. Are intermediate-depth earthquakes in subducting slabs linked to metamorphic dehydration reactions? *J. Geophys. Res.: Solid Earth* **108**, 2030 (2003).
12. Jung, H., Green, H. W. & Dobrzynetska, L. F. Intermediate-depth earthquake faulting by dehydration embrittlement with negative volume change. *Nature* **428**, 545–549 (2004).
13. Okazaki, K. & Hirth, G. Dehydration of lawsonite could directly trigger earthquakes in subducting oceanic crust. *Nature* **530**, 81–84 (2016).
14. Raleigh, C. B. & Paterson, M. S. Experimental deformation of serpentinite and its tectonic implications. *J. Geophys. Res.* **70**, 3965–3985 (1965).
15. Incel, S. et al. Laboratory earthquakes triggered during eclogitization of lawsonite-bearing blueschist. *Earth Planet. Sci. Lett.* **459**, 320–331 (2017).
16. Thielmann, M. Grain size assisted thermal runaway as a nucleation mechanism for continental mantle earthquakes: Impact of complex rheologies. *Tectonophysics* **746**, 611–623 (2018).
17. Ferrand, T. P. Seismicity and mineral destabilizations in the subducting mantle up to 6 GPa, 200 km depth. *Lithos* **334**, 205–230 (2019).
18. Ferrand, T. P. Neither antigorite nor its dehydration is “metastable”. *Am. Mineral.* **104**, 788–790 (2019).
19. Ferrand, T. P. et al. Dehydration-driven stress transfer triggers intermediate-depth earthquakes. *Nat. Commun.* **8**, 15247 (2017).
20. Thielmann, M., Rozel, A., Kaus, B. J. P. & Ricard, Y. Intermediate-depth earthquake generation and shear zone formation caused by grain size reduction and shear heating. *Geology* **43**, 791–794 (2015).
21. Kelemen, P. B. & Hirth, G. A periodic shear-heating mechanism for intermediate-depth earthquakes in the mantle. *Nature* **446**, 787–790 (2007).
22. Prakash, A. et al. Carbonates and intermediate-depth seismicity: Stable and unstable shear in altered subducting plates and overlying mantle. *Proc. Natl Acad. Sci.* **120**, e2219076120 (2023).
23. Ferrand, T. P., Nielsen, S., Labrousse, L. & Schubnel, A. Scaling seismic fault thickness from the laboratory to the field. *J. Geophys. Res.: Solid Earth* **126**, e2020JB020694 (2021).
24. di Toro, G., Hirose, T., Nielsen, S., Pennacchioni, G. & Shimamoto, T. Natural and experimental evidence of melt lubrication of faults during earthquakes. *Science* **311**, 647–649 (2006).
25. Viesca, R. C. & Garagash, D. I. Ubiquitous weakening of faults due to thermal pressurization. *Nat. Geosci.* **8**, 875–879 (2015).
26. Wibberley, C. A. J. & Shimamoto, T. Earthquake slip weakening and asperities explained by thermal pressurization. *Nature* **436**, 689–692 (2005).
27. Burnley, P. C. The importance of stress percolation patterns in rocks and other polycrystalline materials. *Nat. Commun.* **4**, 2117 (2013).
28. Schubnel, A. et al. Deep-focus earthquake analogs recorded at high pressure and temperature in the laboratory. *Science* **341**, 1377–1380 (2013).
29. Jung, H. & Green, H. W. Experimental faulting of serpentinite during dehydration: Implications for earthquakes, seismic low-velocity zones, and anomalous hypocenter distributions in subduction zones. *Int. Geol. Rev.* **46**, 1089–1102 (2004).
30. Mishra, O. P. & Zhao, D. Seismic evidence for dehydration embrittlement of the subducting Pacific slab. *Geophys. Res. Lett.* **31**, L09610 (2004).
31. Wang, J., Zhao, D. & Yao, Z. Seismic anisotropy evidence for dehydration embrittlement triggering intermediate-depth earthquakes. *Sci. Rep.* **7**, 1–9 (2017).
32. Kirby, S. H., Engdahl, R. E. & Denlinger, R. Intermediate-depth intraslab earthquakes and arc volcanism as physical expressions of crustal and uppermost mantle metamorphism in subducting slabs. *Geophys. Monogr.* **96**, 195–214 (1996).
33. Kita, S. & Ferrand, T. P. Physical mechanisms of oceanic mantle earthquakes: Comparison of natural and experimental events. *Sci. Rep.* **8**, 17049 (2018).
34. Ferrand, T. P. & Manea, E. F. Dehydration-induced earthquakes identified in a subducted oceanic slab beneath Vrancea, Romania. *Sci. Rep.* **11**, 10315 (2021).
35. Toffoli, G., Yang, J., Pennacchioni, G., Faccenda, M. & Scambelluri, M. How to quake a subducting dry slab at intermediate depths: Inferences from numerical modelling. *Earth Planet. Sci. Lett.* **578**, 117289 (2022).
36. Zhan, Z. Mechanisms and implications of deep earthquakes. *Ann. Rev. Earth Planet. Sci.* **48**, 147–174 (2020).
37. Fumagalli, P. & Poli, S. Experimentally determined phase relations in hydrous peridotites to 6.5 GPa and their consequences on the dynamics of subduction zones. *J. Petrol.* **46**, 555–578 (2005).
38. Hermann, J. & Lakey, S. Water transfer to the deep mantle through hydrous, Al-rich silicates in subduction zones. *Geology* **49**, 911–915 (2021).
39. Peacock, S. M. & Wang, K. Seismic consequences of warm versus cool subduction metamorphism: Examples from southwest and northeast Japan. *Science* **286**, 937–939 (1999).
40. Scambelluri, M., Cannò, E. & Gilio, M. The water and fluid-mobile element cycles during serpentinite subduction. A review. *Eur. J. Mineral.* **31**, 405–428 (2019).
41. Smit, M. A. & von Strandmann, P. A. E. P. Deep fluid release in warm subduction zones from a breached slab seal. *Earth Planet. Sci. Lett.* **534**, 116046 (2020).
42. Till, C. B., Grove, T. L. & Withers, A. C. The beginnings of hydrous mantle wedge melting. *Contrib. Mineral. Petrol.* **163**, 669–688 (2012).
43. Pawley, A. Chlorite stability in mantle peridotite: The reaction clinocllore + enstatite = forsterite + pyrope + H₂O. *Contrib. Mineral. Petrol.* **144**, 449–456 (2003).
44. Staudigel, H. & Schreyer, W. The upper thermal stability of clinocllore, Mg₅Al [AlSi₃O₁₀](OH)₈, at 10–35 kb PH₂O. *Contrib. Mineral. Petrol.* **61**, 187–198 (1977).
45. Dey, A., Choudhury, S. R., Mukherjee, S., Sanyal, S. & Sengupta, P. Origin of vesuvianite-garnet veins in calc-silicate rocks from part of the Chotanagpur Granite Gneiss Complex, East Indian Shield: The quantitative P-T-XCO₂ topology in parts of the system CaO-MgO-Al₂O₃-SiO₂-H₂O-CO₂ (+Fe₂O₃, F). *Am. Mineral.: J. Earth Planet. Mater.* **104**, 744–760 (2019).
46. Hacker, B. R., Abers, G. A. & Peacock, S. M. Subduction factory 1. Theoretical mineralogy, densities, seismic wave speeds, and H₂O contents. *J. Geophys. Res. Solid Earth* **108**, 2029 (2003).
47. Dobson, D. P., Meredith, P. G. & Boon, S. A. Simulation of subduction zone seismicity by dehydration of serpentinite. *Science* **298**, 1407–1410 (2002).
48. Wong, T.-F., Ko, S.-C. & Olgaard, D. L. Generation and maintenance of pore pressure excess in a dehydrating system 2. Theoretical analysis. *J. Geophys. Res.: Solid Earth* **102**, 841–852 (1997).
49. Craiu, A., Ferrand, T. P., Manea, E. F., Vrijmoed, J. C. & Mărmureanu, A. A switch from horizontal compression to vertical extension in the Vrancea slab explained by the volume reduction of serpentinite dehydration. *Sci. Rep.* **12**, 22320 (2022).
50. Ferrand, T. P. et al. Energy balance from a mantle pseudotachylyte, Balmuccia, Italy. *J. Geophys. Res.: Solid Earth* **123**, 3943–3967 (2018).
51. Ohuchi, T. et al. In situ X-ray and acoustic observations of deep seismic faulting upon phase transitions in olivine. *Nat. Commun.* **13**, 5213 (2022).
52. Ohuchi, T., Lei, X., Higo, Y., Tange, Y. & Sakai, T. Switching from seismic faulting to silent slips in harzburgite induced by H₂O fluid at upper mantle pressures. *Contrib. Mineral. Petrol.* **175**, 1–19 (2020).
53. Gasc, J. et al. Ductile vs. Brittle Strain localization induced by the Olivine-Ringwoodite transformation. *Minerals* **12**, 719 (2022).
54. Mao, G. L. et al. Unsupervised machine learning reveals slab hydration variations from deep earthquake distributions beneath the northwest Pacific. *Commun. Earth Environ.* **3**, 56 (2022).
55. Magott, R., Fabbri, O. & Fournier, M. Seismically-induced serpentinite dehydration as a possible mechanism of water release in subduction zones. Insights from the Alpine Corsica pseudotachylyte-bearing Monte Maggiore ophiolitic unit. *Lithos* **362**, 105474 (2020).
56. Fang, H. & van der Hilst, R. D. Earthquake depth phase extraction with P wave autocorrelation provides insight into mechanisms of intermediate-depth earthquakes. *Geophys. Res. Lett.* **46**, 14440–14449 (2019).
57. Florez, M. A. & Prieto, G. A. Controlling factors of seismicity and geometry in double seismic zones. *Geophys. Res. Lett.* **46**, 4174–4181 (2019).
58. Peacock, S. M. Are the lower planes of double seismic zones caused by serpentinite dehydration in subducting oceanic mantle? *Geology* **29**, 299–302 (2001).

59. Han, P., Wei, D., Zhang, K., Sun, Z. & Zhou, X. Lattice-preferred orientations of olivine in subducting oceanic lithosphere derived from the observed seismic anisotropies in double seismic zones. *Earthq. Sci.* **29**, 243–258 (2016).
60. Sippl, C., Dielforder, A., John, T. & Schmalholz, S. M. Global constraints on intermediate-depth intraslab stresses from slab geometries and mechanisms of double seismic zone earthquakes. *Geochem. Geophys. Geosyst.* **23**, e2022GC010498 (2022).
61. Kim, D. & Jung, H. Deformation microstructures of olivine and chlorite in chlorite peridotites from Almklovdalen in the Western Gneiss Region, southwest Norway, and implications for seismic anisotropy. *Int. Geol. Rev.* **57**, 650–668 (2015).
62. Morales, L. F. G., Mainprice, D. & Boudier, F. The influence of hydrous phases on the microstructure and seismic properties of a hydrated mantle rock. *Tectonophysics* **594**, 103–117 (2013).
63. Alt, J. C. et al. Recycling of water, carbon, and sulfur during subduction of serpentinites: A stable isotope study of Cerro del Almiraz, Spain. *Earth Planet. Sci. Lett.* **327**, 50–60 (2012).
64. Lee, J., Jung, H., Klemd, R., Tarling, M. S. & Konopelko, D. Lattice preferred orientation of talc and implications for seismic anisotropy in subduction zones. *Earth Planet. Sci. Lett.* **537**, 116178 (2020).
65. Getting, I. C. & Kennedy, G. C. Effect of pressure on the emf of chromel-alumel and platinum-platinum 10% rhodium thermocouples. *J. Appl. Phys.* **41**, 4552–4562 (1970).
66. Mirwald, P. W., Getting, I. C. & Kennedy, G. C. Low-friction cell for piston-cylinder high-pressure apparatus. *J. Geophys. Res.* **80**, 1519–1525 (1975).
67. Ko, B. & Jung, H. Crystal preferred orientation of an amphibole experimentally deformed by simple shear. *Nat. Commun.* **6**, 6586 (2015).
68. de Capitani, C. & Petrakakis, K. The computation of equilibrium assemblage diagrams with Theriak/Domino software. *Am. Mineral.* **95**, 1006–1016 (2010).
69. Holland, T. J. B. & Powell, R. An improved and extended internally consistent thermodynamic dataset for phases of petrological interest, involving a new equation of state for solids. *J. Metamorph. Geol.* **29**, 333–383 (2011).
70. Holland, T. J. B., Baker, J. & Powell, R. Mixing properties and activity-composition relationships of chlorites in the system MgO-FeO-Al₂O₃-SiO₂-H₂O. *Eur. J. Mineral.* **10**, 395–406 (1998).
71. Holland, T. J. B. & Powell, R. An internally consistent thermodynamic data set for phases of petrological interest. *J. Metamorph. Geol.* **16**, 309–343 (1998).
72. Holland, T. J. B. & Powell, R. Thermodynamics of order-disorder in minerals: II. Symmetric formalism applied to solid solutions. *Am. Mineral.* **81**, 1425–1437 (1996).
73. White, R. W., Powell, R. & Holland, T. J. B. Progress relating to calculation of partial melting equilibria for metapelites. *J. Metamorph. Geol.* **25**, 511–527 (2007).
74. Diener, J. F. A. & Powell, R. Revised activity-composition models for clinopyroxene and amphibole. *J. Metamorph. Geol.* **30**, 131–142 (2012).
75. Powell, R. & Holland, T. J. B. Relating formulations of the thermodynamics of mineral solid solutions: Activity modeling of pyroxenes, amphiboles, and micas. *Am. Mineral.* **84**, 1–14 (1999).
76. Locock, A. J. An Excel spreadsheet to classify chemical analyses of amphiboles following the IMA 2012 recommendations. *Comput. Geosci.* **62**, 1–11 (2014).

Acknowledgements

The authors are grateful to the editor and reviewers Dr. Thomas P. Ferrand and an anonymous reviewer, whose suggestions and comments have notably improved the manuscript. Permission to collect starting material was not required. This research was funded by the National Research Foundation of Korea (NRF: 2020R1A2C2003765 and 2022R1A5A1085103) to H.J. and partially by Korea Polar Research Institute (KOPRI: PE23050) to D.K.

Author contributions

D.K. and H.J. conceived the study. D.K. conducted experiments and wrote the manuscript under supervision of H.J. D.K. analysed data under contribution of J.L. All authors contributed to editing and discussion of the paper.

Competing interests

The authors declare no competing interests.

Additional information

Supplementary information The online version contains supplementary material available at <https://doi.org/10.1038/s43247-023-01133-5>.

Correspondence and requests for materials should be addressed to Haemyeong Jung.

Peer review information *Communications Earth & Environment* thanks Thomas Ferrand and the other, anonymous, reviewer(s) for their contribution to the peer review of this work. Primary Handling Editors: Sylvain Barbot and Joe Aslin. A peer review file is available.

Reprints and permission information is available at <http://www.nature.com/reprints>

Publisher's note Springer Nature remains neutral with regard to jurisdictional claims in published maps and institutional affiliations.



Open Access This article is licensed under a Creative Commons Attribution 4.0 International License, which permits use, sharing, adaptation, distribution and reproduction in any medium or format, as long as you give appropriate credit to the original author(s) and the source, provide a link to the Creative Commons licence, and indicate if changes were made. The images or other third party material in this article are included in the article's Creative Commons licence, unless indicated otherwise in a credit line to the material. If material is not included in the article's Creative Commons licence and your intended use is not permitted by statutory regulation or exceeds the permitted use, you will need to obtain permission directly from the copyright holder. To view a copy of this licence, visit <http://creativecommons.org/licenses/by/4.0/>.

© The Author(s) 2023